Journal of The Electrochemical Society, **156** (6) B682-B689 (2009)
0013-4651/2009/156(6)/B682/8/$25.00 © The Electrochemical Society

Advanced Electrochemical Properties of $LnBa_{0.5}Sr_{0.5}Co_2O_{5+\delta}$ (Ln = Pr, Sm, and Gd) as Cathode Materials for IT-SOFC

Jung Hyun Kim,[a] Mark Cassidy,[b,*] John T. S. Irvine,[b,*,z] and Joongmyeon Bae[a,z]

[a]*Department of Mechanical Engineering, Korea Advanced Institute of Science and Technology, Daejeon 305-701, Korea*
[b]*School of Chemistry, University of St. Andrews, St. Andrews, Fife KY16 9ST, United Kingdom*

Excellent area-specific-resistance (ASR) values have been exhibited by cathode materials with a Sr-doped layer perovskite type structure and therefore show themselves to be possible candidates for intermediate-temperature-operating solid oxide fuel cell (IT-SOFC, 600–800°C) applications. $SmBa_{0.5}Sr_{0.5}Co_2O_{5+\delta}$ (SBSCO) electrode was sintered onto 10 mol % gadolinia-doped ceria ($Ce_{0.9}Gd_{0.1}O_2$, CGO91) at 1000°C to form symmetrical cells and exhibited an ASR value of 0.092 Ω cm^2 at 700°C. The lowest ASR value was observed when the composite cathode of 50 wt % of SBSCO and 50 wt % of CGO91 (SBSCO50) was used in conjunction with an interlayer of CGO91 applied between the electrode and 8 mol % Y_2O_3 stabilized ZrO_2 electrolyte. These were 0.12 Ω cm^2 at 600°C and 0.019 Ω cm^2 at 700°C, respectively. The coefficient of thermal expansion (CTE) of SBSCO was 21.9×10^{-6} K^{-1} at 700°C. However, the CTE of the composite cathode of SBSCO50 was shown to be 13.6×10^{-6} K^{-1} at 700°C, this being more compatable with the other components within the cell.
 [DOI: 10.1149/1.3110989]

Manuscript submitted November 14, 2008; revised manuscript received February 11, 2009. Published April 6, 2009.

Cathode overpotential can be a major source of voltage loss in solid oxide fuel cells (SOFCs) and becomes even more significant as the operating temperatures are reduced to allow the use of metal interconnects and simplify system design. For practical fuel cell operation, a target power density of 0.5 W cm^{-2} at 0.7 V is required at the specific operating point of any SOFC.[1] This requirement leads to an estimated area specific resistance (ASR) of 0.15 Ω cm^2 as a target value for an SOFC cathode.

Much of the research on cathode materials for SOFCs has been devoted to the perovskite oxide $La_{1-x}Sr_xMnO_{3-\delta}$ (LSM), and this is the most widely used cathode material due to its good thermal and chemical stability.[2] However, LSM does not provide adequate performance for intermediate-temperature SOFCs (IT-SOFCs) because of its lower catalytic activity and electrical conductivity at an operating temperature range from 600 to 800°C which increases cathode polarization.[3,4] $La_{1-x}Sr_xCoO_{3-\delta}$ (LSC) has been shown to have a higher catalytic activity than LSM for the reduction of oxygen; further, higher levels of ionic conductivity result in mixed-conducting oxides which also aid the reduction in polarization resistance at intermediate temperature ranges.[5]

Recently, several research groups have reported excellent cathode behavior using materials with a layered perovskite (LP) structure.[6-9] These materials have an orthorhombic symmetry displaying two types of Co–O environment, Co–O_5 square pyramids and Co–O_6 octahedra, which alternate along the *b* axis.[6,7] Chang et al. investigated the electrochemical properties of $GdBaCo_2O_{5+\delta}$ (GBCO) for IT-SOFC applications and reported an ASR value of 0.534 Ω cm^2 at 650°C.[8] The oxygen ion diffusivity and surface exchange coefficient of $PrBaCo_2O_{5+\delta}$ (PBCO) were characterized by Kim et al.[9] and shown to be about 10^{-5} cm^2 s^{-1} and 10^{-3} cm s^{-1}, respectively, at 350°C. These values are 2–3 orders of magnitude higher than that of $La_{0.5}Sr_{0.5}FeO_{3-\delta}$ or $La_{0.5}Sr_{0.5}CoO_{3-\delta}$. Significantly, it also exhibited a conductivity of 900 S cm^{-1} at 500°C and 600 S cm^{-1} at 700°C with a metallic behavior. The ASR value of composite cathodes with PBCO on a $Ce_{0.9}Gd_{0.1}O_{2-\delta}$ (CGO91) electrolyte was about 0.15 Ω cm^2 at 600°C.

To date, these excellent properties have been attained on straightforward layered perovskite materials with the general formula $A'A''B_2O_{5+\delta}$, where the A″ cation is generally Ba. Some initial investigations have been carried out investigating the substitution of the Ba cation with Sr to form a double-layered perovskite; however, this work was focused on characterization of basic structure and initial performance.[10,11]

The objective of this work was to build on these initial studies and investigate the structural characteristics, electrochemical properties, and thermal expansion behavior of the Sr-doped LP (S-LP) oxide system $LnBa_{0.5}Sr_{0.5}Co_2O_{5+\delta}$ (where Ln = Pr, Sm, and Gd) for IT-SOFC cathode applications.

Experimental

Sample preparation, X-ray diffraction measurement, and microstructure analysis.— Lanthanide oxides (Pr_6O_{11}, Sm_2O_3, and Gd_2O_3), barium carbonate ($BaCO_3$), strontium carbonate ($SrCO_3$), and cobalt oxide (Co_3O_4) were used for cathode synthesis. Stoichiometric amounts of these raw powders were mixed and ground in a mortar and pestle. These were then placed in a muffle furnace and heated using various ramp rates from room temperature to 1000°C for 8 h as a first calcination in order to decompose the carbonate. Samples were then ballmilled (roller type) for 24 h with zirconia milling media in acetone before a second heat-treatment of 1100°C for 36 h was applied, after which samples were cooled to room temperature. The abbreviations used to identify the various samples are summarized in Table I.

Table I. Abbreviations of specimens.

Chemical composition	Abbreviations
$Ce_{0.9}Gd_{0.1}O_{2-\delta}$	CGO91
$PrBa_{0.5}Sr_{0.5}Co_2O_{5+\delta}$	PBSCO
$SmBa_{0.5}Sr_{0.5}Co_2O_{5+\delta}$	SBSCO
$GdBa_{0.5}Sr_{0.5}Co_2O_{5+\delta}$	GBSCO
$SmBa_{0.5}Sr_{0.5}Co_2O_{5+\delta}$(90 wt %) and $Ce_{0.9}Gd_{0.1}O_{2-\delta}$(10 wt %)	SBSCO10
$SmBa_{0.5}Sr_{0.5}Co_2O_{5+\delta}$(80 wt %) and $Ce_{0.9}Gd_{0.1}O_{2-\delta}$(20 wt %)	SBSCO20
$SmBa_{0.5}Sr_{0.5}Co_2O_{5+\delta}$(70 wt %) and $Ce_{0.9}Gd_{0.1}O_{2-\delta}$(30 wt %)	SBSCO30
$SmBa_{0.5}Sr_{0.5}Co_2O_{5+\delta}$(60 wt %) and $Ce_{0.9}Gd_{0.1}O_{2-\delta}$(40 wt %)	SBSCO40
$SmBa_{0.5}Sr_{0.5}Co_2O_{5+\delta}$(50 wt %) and $Ce_{0.9}Gd_{0.1}O_{2-\delta}$(50 wt %)	SBSCO50

* Electrochemical Society Active Member.
z E-mail: jtsi@st-andrews.ac.uk; jmbae@kaist.ac.kr

The X-ray diffraction (XRD) patterns of the prepared samples were obtained in a Philips diffractometer using Cu radiation (λ = 0.15418 nm). The obtained data were matched with reference data for the identification of crystal structures.

The microstructure of a symmetrical half-cell was investigated using field-emission scanning electron microscopy (SEM, S-4200, Hitachi) combined with energy-dispersive spectroscopy.

Thermal-expansion behaviors.— The pellets for thermal-expansion behavior of S-LP oxide were sintered at 1100°C for 12 h in air. Specimen geometry was a rectangular-shaped bar type (5 × 5 × 18 mm). The coefficient of thermal expansion (CTE) of the samples was measured with a NETZSCH DIL 402C Dilatometer from room temperature to 1000°C with a heating rate of 5°C/min.

Electrochemical characterization.— CGO91 (10 mol % Praxair Specialty Ceramics) and 8 mol % Y_2O_3 stabilized ZrO_2 (8YSZ, Tosoh) were used for electrolytes. These were prepared by pressing the powders into pellets with circular shapes at 2×10^3 kg/m^2 and sintering at 1400°C for 4 h. In order to prevent the formation of undesired phases between the cobalt-based perovskite materials and 8YSZ, a double-layered electrolyte (DLE) was fabricated using a CGO91 slurry coating applied by spin coater to the surface of the 8YSZ before final electrolyte firing. The final geometry of sintered electrolyte pellets was approximately 21 mm in diameter and 2 mm in thickness.

Single-phase cathodes and composite cathodes with CGO91 were used for electrochemical measurements. Suitable inks were made by mixing powders with an appropriate solvent and binder system; electrodes were then applied to the electrolytes using screen printing to form symmetrical half-cells. These were sintered for 1 h at 900–1200°C in order to form a porous electrode structure well-bonded to the electrolyte. The final surface area of the symmetric cell was about 1.09 cm^2.

The measurements of electrochemical properties and ASRs of the cathodes were performed at open-circuit voltage in air as a function of temperature between 500 and 850°C with an increment of 50°C. AC impedance characteristics were measured with a Solatron 1260 frequency analyzer over a frequency range of 0.01 Hz to 1 MHz and an amplitude of 50 mV. The cathode polarization was determined from the differences of the low- and high-frequency intercept on the impedance curves and divided by 2.

Result and Discussion

XRD results of $PrBa_{0.5}Sr_{0.5}Co_2O_{5+\delta}$ (PBSCO), $SmBa_{0.5}Sr_{0.5}Co_2O_{5+\delta}$ (SBSCO), and $GdBa_{0.5}Sr_{0.5}Co_2O_{5+\delta}$ (GBSCO) are shown in Fig. 1. All compositions are identified as a single phase. However the use of different lanthanide cations such as Pr, Sm, and Gd on the A site of S-LP results in different XRD behavior. When Pr is used with fixed Ba, Sr, and Co, the peaks from 10 to 90° (2θ) do not split, whereas those for Gd and Sm split.

The structures of cobalt-based LPs with different-sized rare earths can exist in either tetragonal or orthorhombic forms.[12,13] When the larger (Pr and Nd) or smaller (Dy and Ho) are used, the structures of $LnBaCo_2O_{5+\delta}$ (Ln: Pr, Dy, and Ho) are identified as tetragonal. In contrast, for the intermediate-size cation (Sm, Eu, Gd, and Tb), a much larger orthorhombic distortion is observed.[12,13] In the XRD results presented in Fig. 1, the subcell is pseudotetragonal for the larger cation (Pr). In contrast, for the intermediate-size cations (Sm and Gd), a much larger orthorhombic distortion is observed due to the difference of the atomic ionic radii leading to distortion of the structure of the S-LP sublattice.[11,14] The XRD patterns of SBSCO and GBSCO are similar to those reported for $SmBaCo_2O_{5+\delta}$ and GBCO.[8,12]

In order to investigate the reactivity of SBSCO and 8YSZ, mixtures of the two were heat-treated for 1 h at various temperatures between 900 and 1200°C and the phase composition analyzed by XRD. The results are shown in Fig. 2 and reveal that a reaction between SBSCO and 8YSZ occurs above 900 °C. It shows that

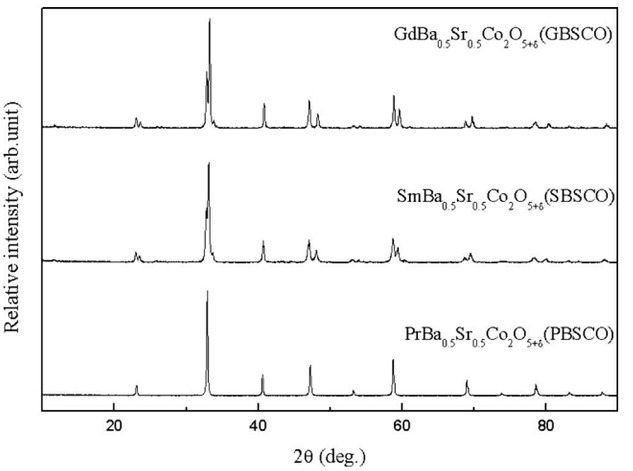

Figure 1. XRD patterns of $LnBa_{0.5}Sr_{0.5}Co_2O_{5+\delta}$ (Ln: Pr, Sm, and Gd) oxides calcined at 1100°C for 36 h.

SBSCO is therefore unsuitable as a cathode in direct-contact 8YSZ electrolyte where temperatures of processing or operation exceed 1000°C. Generally, LSC oxide reacts with 8YSZ above 1000°C and results in secondary phases such as $La_2Zr_2O_7$ or $SrZrO_3$.[15-18] The secondary phase in Fig. 2 was matched to $SrZrO_3$ (PDF no. 00-023-0561 and 00-031-1365), indicated with an open circle- however, the phase of $Sm_2Zr_2O_7$ was not found. The peak with a black arrow is the secondary phase of Co_3O_4.[19,20] The peak showing a black closed square is an unidentified phase from the reaction between SBSCO and 8YSZ that occurs at 1200°C.

The reactivity of CGO91 and SBSCO mixtures was investigated in the same way as before (Fig. 3). While no apparent secondary or unknown products were observed up to a heating temperature of 1100°C, a weak reflection caused by an unknown phase appeared on heating at 1200°C. This phase can be related to the interdiffusion of the two lattices, particulary the migration of Sr and Co from SBSCO to the grain boundaries of the ceria.[21] These results show that SBSCO must be used on Ce-based electrolytes for IT-SOFC applications, or where in conjunction with an 8YSZ electrolyte, Ce-based barrier layers must be considered to prohibit the secondary phase generation.

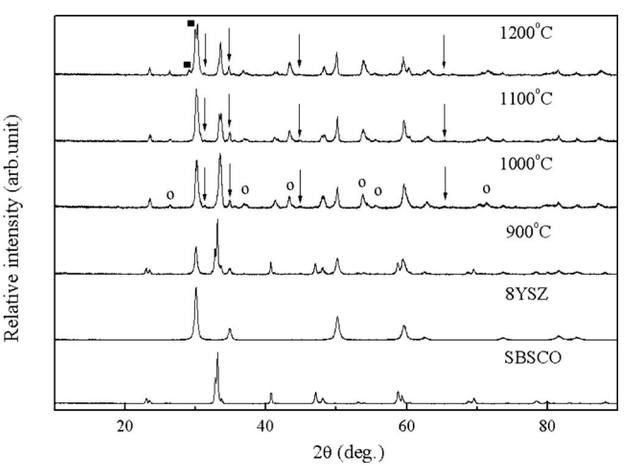

Figure 2. XRD patterns of a mixture of 8YSZ and SBSCO sintered from 900 to 1200°C for 1 h. The black open circle and black arrow are the secondary phase between SBSCO and 8YSZ and considered as $SrZrO_3$ and Co_3O_4 from references. The black closed square is an unknown phase from these experiments.

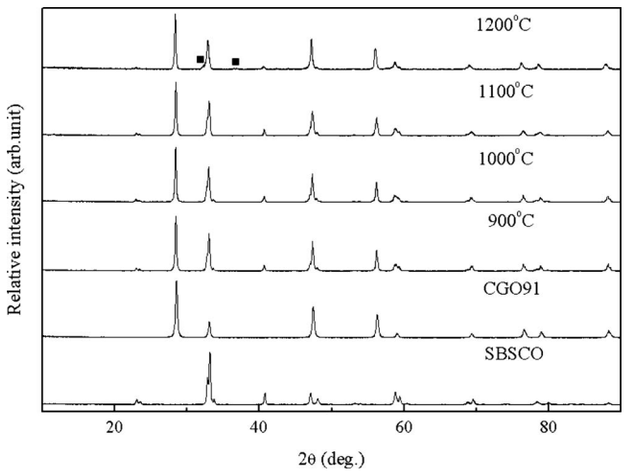

Figure 3. XRD patterns of mixture of CGO91 and SBSCO sintered from 900 to 1200°C for 1 h. The black closed square is an unknown phase from these experiments.

The effects of sintering on the ASR of PBSCO, SBSCO, and GBSCO cathodes on CGO91 electrolyte are shown in Fig. 4. A sintering temperature of 1000°C for 1 h results in the lowest ASR value in all of the compositions, which can be related to the microstructures shown in Fig. 5 and 6. The SEM images in Fig. 5 show the top surface of SBSCO. One can see many cracks on the surface of the specimen sintered at 900°C (Fig. 5a and b) as well as specimens sintered at 1100°C (Fig. 5e and f) and 1200°C (Fig. 5g and h); these appear to be at a minimum on the 1000°C (Fig. 5c and d) specimen. The presence of this cracking will have a detrimental impact on current collection and distribution within the electrode. Fracture cross sections of the SBSCO cathode are shown in Fig. 6a-h. From these figures, it can be seen that the specimen sintered at 900°C shows relatively poor adhesion between the cathode and CGO91 and was easily peeled off. Better adhesion was observed when specimens were sintered above 1000°C. However, as the sintering temperature increased toward 1200°C, the electrode microstructure became increasingly dense, which results in a reduced surface area for exchange of reaction species and possible mass-transport losses. In summary, it can be suggested that a sintering temperature of 1000°C provides the best balance between the conflicting electrode requirements of maintaining a porous, high-surface-area structure while at the same time providing a strong, well-sintered, and adherent layer. At 900°C, the temperature is not high enough to result in a structure of sufficient particle necking for good contact and adhesion, while at higher temperatures, surface area is lost and more shrinkage cracking is observed. It must also be mentioned that this optimal temperature has a strong relationship to the starting morphology of the powder.

ASR results with Arrhenius plots of PBSCO, SBSCO, and GBSCO sintered at 1000°C on CGO91 electrolyte are shown in Fig. 7a. Comparing the ASR of PBSCO, SBSCO, and GBSCO, the SBSCO is the lowest at all the temperatures tested, with values of 0.092 Ω cm^2 at 700°C and 0.244 Ω cm^2 at 650°C in Fig. 7b. This compares well with the value of 0.602 Ω cm^2 at 650°C for GBCO reported by Chang et al.,[8] with SBSCO showing about half the ASR of that of GBCO. Significantly, the impact of Sr substitution can be compared GBSCO and GBCO[8] sintered at 1000°C. The ASRs of GBCO on $Ce_{0.8}Gd_{0.2}O_{2-\delta}$ were 15.040, 4.870, 1.730, and 0.602 Ω cm^2 at 499, 549, 598, and 645°C. However, the ASRs of GBSCO shown in Fig. 7 are 6.875, 3.484, 1.252, and 0.558 Ω cm^2 at 500, 550, 600, and 650°C. These comparisons indicate that the Sr substitution in LP results in decreased polarization resistance.

Comparison of the results of PBSCO, SBSCO, and GBSCO as well as GBCO[8] and GBSCO indicates that S-LP oxide with Sm substitution reduces the ASR value and may be related to fast oxygen diffusion in the bulk and high surface kinetics on the surface of electrode.[9] Activation energies of PBSCO, SBSCO, and GBSCO were determined from the Arrhenius plot of Fig. 7a and were 1.07, 1.23, and 1.22 eV, respectively. These values are consistantly lower than that of GBCO (1.34 eV).[8]

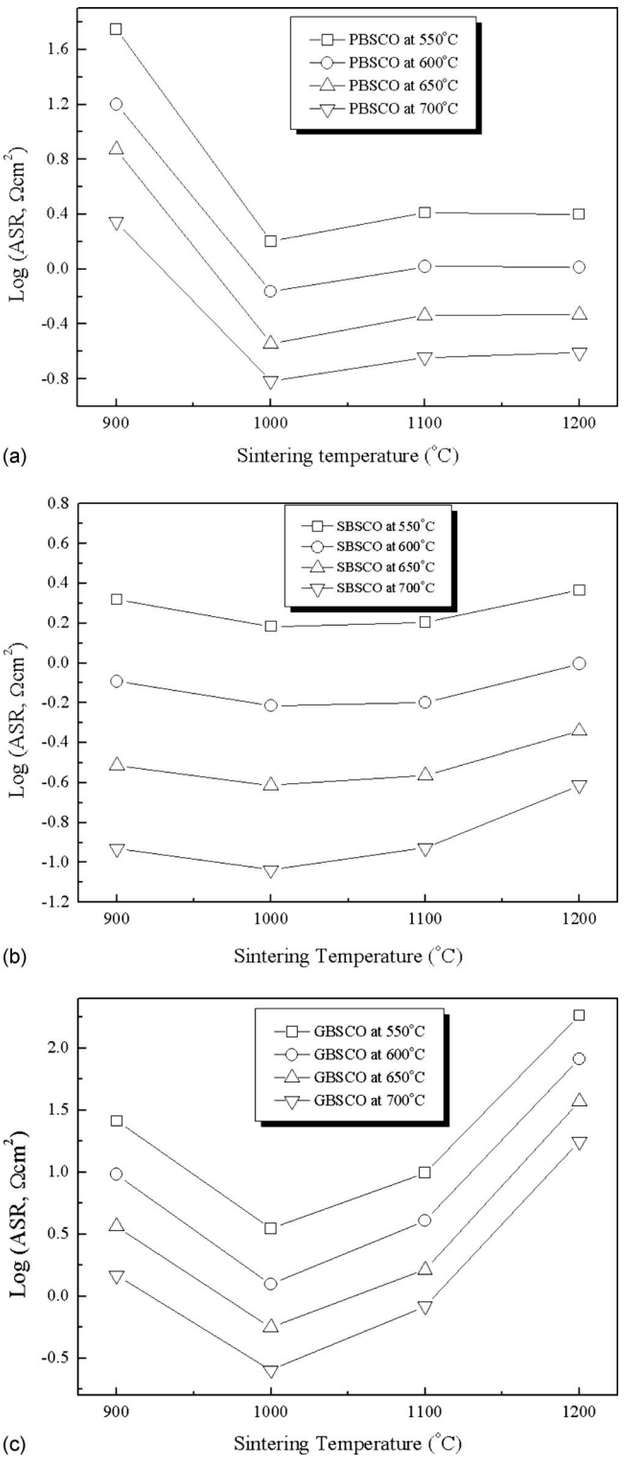

Figure 4. ASR results shown as Arrhenius plot of (a) PBSCO, (b) SBSCO, and (c) GBSCO on the CGO91 electrolyte with respect to the sintering temperature. Sintering temperature of symmetrical half-cell was kept for 1 h at specific temperature.

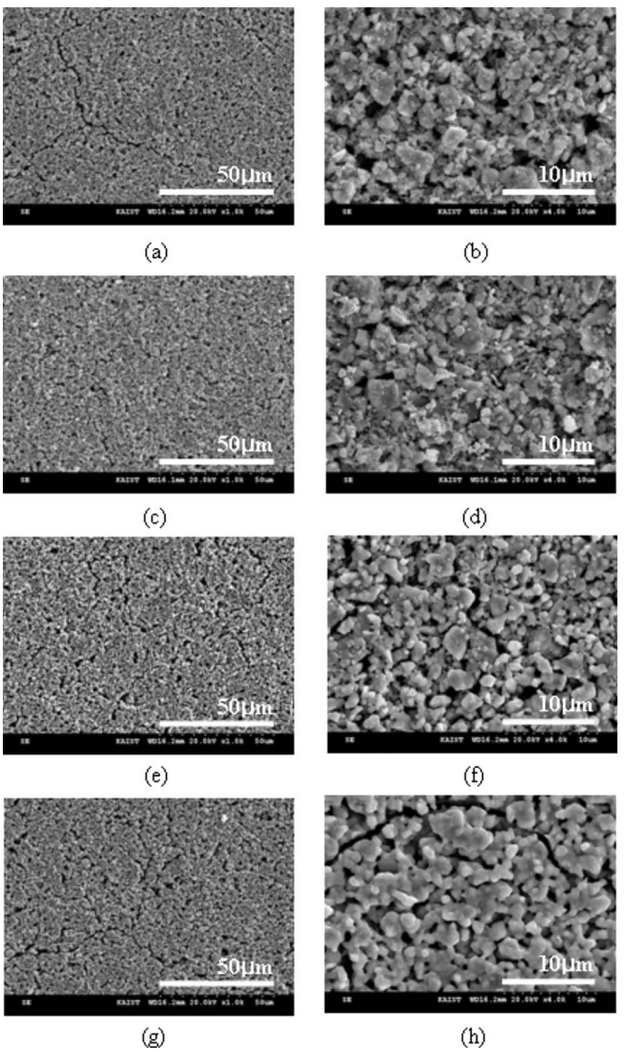

Figure 5. SEM images of top view in SBSCO. The specimen is (a), and (b) is the top view of symmetric cell sintered at 900°C. The other samples of (c)-(d), (e)-(f), and (g)-(h) are sintered at 1000, 1100, and 1200°C for 1 h.

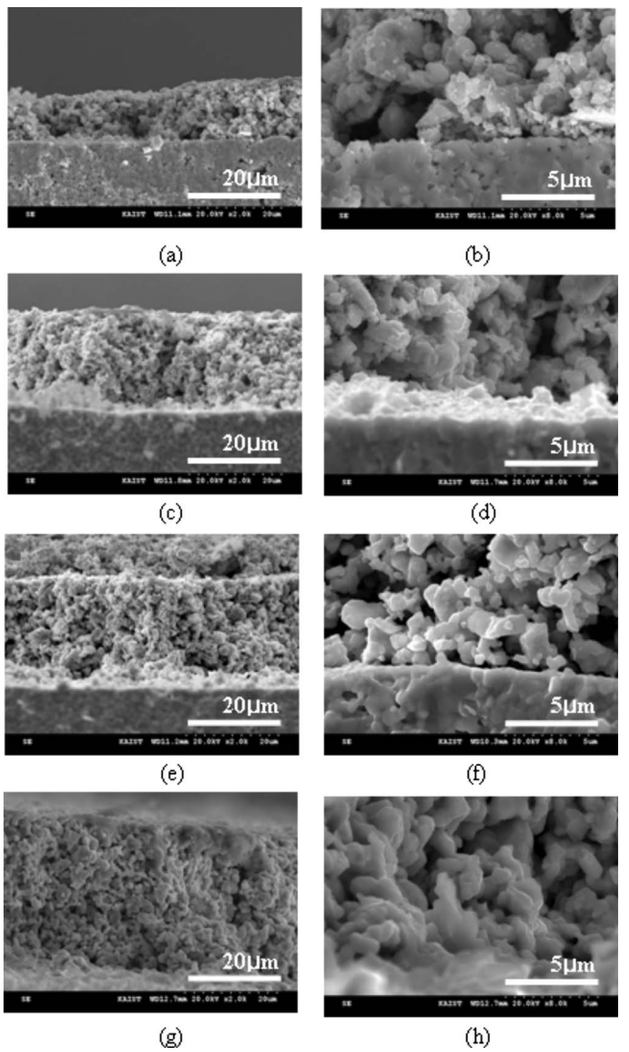

Figure 6. SEM images of cross view in SBSCO. The specimen is (a), and (b) is the top view of symmetric cell sintered at 900°C. The other samples of (c)-(d), (e)-(f), and (g)-(h) are sintered from 1000 to 1200°C for 1 h.

The ASR results of SBSCO with respect to various electrolyte materials are summarized in Fig. 8. The electrolytes used were CGO91, 8YSZ, and the DLE; the numbers in the bracket indicate sintering temperature of the coating for 1 h. From these results it can be seen that the SBSCO on the DLE exhibited the lowest ASR value (0.033 Ω cm^2, at 700°C). SBSCO(1000) on DLE showed a value 2 orders of magnitude lower than that of SBSCO(1000) on 8YSZ over the complete temperature range. The presence of the CGO91 on the surface of 8YSZ not only prohibits the secondary phase formation between the SBSCO and 8YSZ but also increases the triple-phase-boundary contact of SBSCO through the relatively porous CGO91 microstructure. This can be seen in Fig. 9, where the CGO91 layer does not have a smooth geometry such as the electrolyte but rather a relatively rugged surface, which results in an increased area of contact between SBSCO and the CGO91. It is most likely a combination of both chemical barrier and microstructural enhancement that result in the lowest ASR value for the DLE specimens.

The effect of sintering temperature on the performance of the DLE specimens was also evident in Fig. 8. The ASR of SBSCO(1100) on DLE was 7.752 Ω cm^2 at 700°C and 0.033 Ω cm^2 in the case of SBSCO(1000) on DLE. The difference of 2 orders of magnitude in ASR between the two samples was due not only to the microstructural changes shown in Fig. 5 and 6, where the higher sintering temperature leads to a denser electrode and more cracking, both of which result in higher polarizations, but also to reaction between the materials as observed previously in Fig. 2 and 3. In the case of reaction, the high sintering temperature can generate reaction between SBSCO and CGO91. This further suggests that the optimal sintering temperature in the case of the DLE condition can be considered at 1000°C.

Figure 10 shows the impedance results of various composite cathodes at 700°C with varying ratios of SBSCO to CGO91 from 100% SBSCO to a 50:50 mixture of the two components. These results show that the lowest polarization resistance was obtained at the 50:50 ratio and is in line with the current model[22] of composite cathodes, in that this provides the maximum triple phase boundary for electrochemical exchange. However, this advantage is only realized once the secondary phase has become percolating, allowing the full extent of the increased triple phase boundary to be utilized.

The ASRs of these composite cathodes with respect to temperature are summarized in Fig. 11a. The ASR values did not correspond directly to the ratio of SBSCO and CGO91 in the composite and decreased in sequence of SBSCO20 (80 wt % of SBSCO and

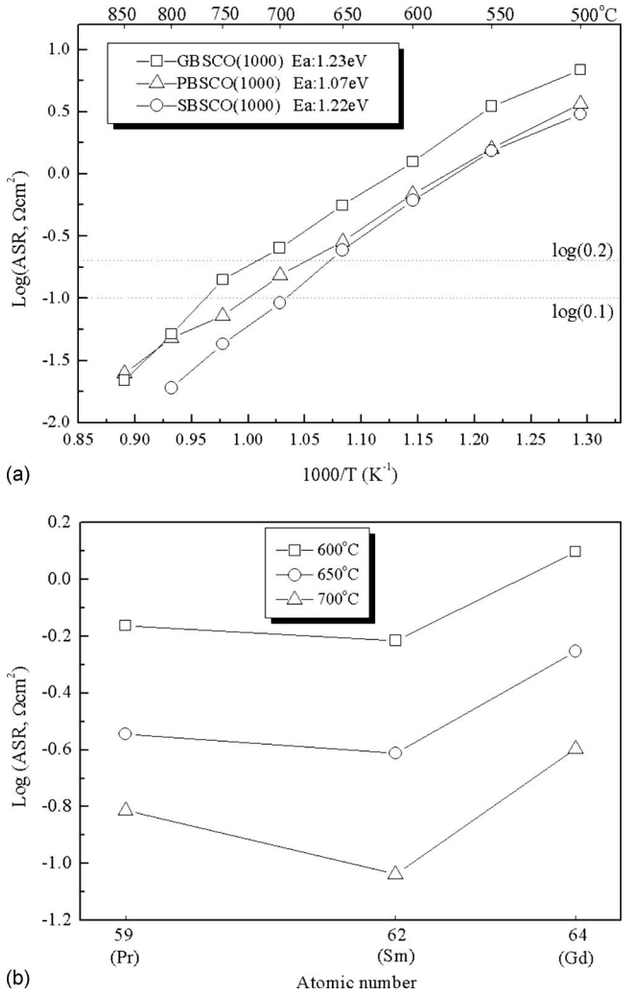

Figure 7. (a) ASR results shown as Arrhenius plot of $LnBa_{0.5}Sr_{0.5}Co_2O_{5+\delta}$ (Ln: Pr, Sm, and Gd) on CGO91 electrolyte. The number in the bracket indicates that these specimens were sintered at 1000°C for 1 h on CGO91. (b) ASR results with lanthanide atomic number at 600, 650 and 700°C.

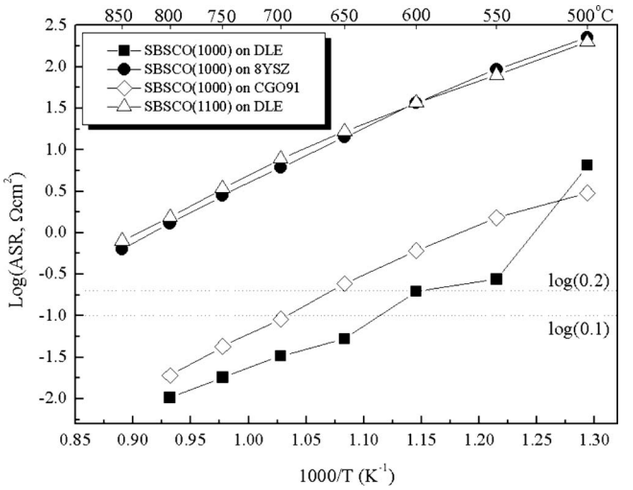

Figure 8. ASR results of SBSCO on various electrolytes from 500 to 850°C. DLE is composed of coated CGO91 on the side of 8YSZ. The numbers in the bracket indicates sintering temperature for 1 h.

20 wt % of CGO91), SBSCO10 (90 wt % of SBSCO and 10 wt % of CGO91), SBSCO30 (70 wt % of SBSCO and 30 wt % of CGO91), SBSCO, SBSCO40 (60 wt % of SBSCO and 40 wt % of CGO91), and SBSCO50 (50 wt % of SBSCO and 50 wt % of CGO91). From SBSCO20 to SBSCO50 in Fig. 11b, these compositions are consistent with the percolation effects discussed above. Below the percolation limit, the addition of the CGO91 merely disrupts the conduction in the electrode, leading to a higher observed resistance; as it reaches the percolation threshold, the full triple-phase-boundary network is able to contribute to the electrochemical processes, resulting in a reduced polarization. As the CGO91 level continues to increase, one would expect polarization resistance (*Rp*) to begin to rise as the percolation in the SBSCO phase begins to become disrupted by the high levels of CGO91. One would expect a minimum *Rp* at around a 50 wt % mixture of the two phases, where the best balance of maximum triple phase boundary and percolation in both phases would exist. The exact position of this minimum would, of course, show a strong dependency on microstructure, defined by such effects as particle size distribution and surface area of the starting powders and process parameters such as sintering temperature and composite thickness.

Of note is the ASR of the CGO91:SBSCO composite at 600°C with values of 0.15 and 0.12 Ω cm^2 at 40 and 50 wt % CGO91, respectively. When compared to the ASR of the PBCO:CGO91 composite, the ASR of the SBSCO50 was 20% lower than that of the PBCO:CGO91 composite.[9] From these results SBSCO50 can be considered a candidate cathode material for SOFC applications at 600°C.[23] Also, the ASR value of the SBSCO50 used on the DLE structure based on 8YSZ was shown to have lowest value when compared to other cathode materials,[24-26] suggesting that it could be possible to generate high power density at 600°C using conventional electrolyte materials.

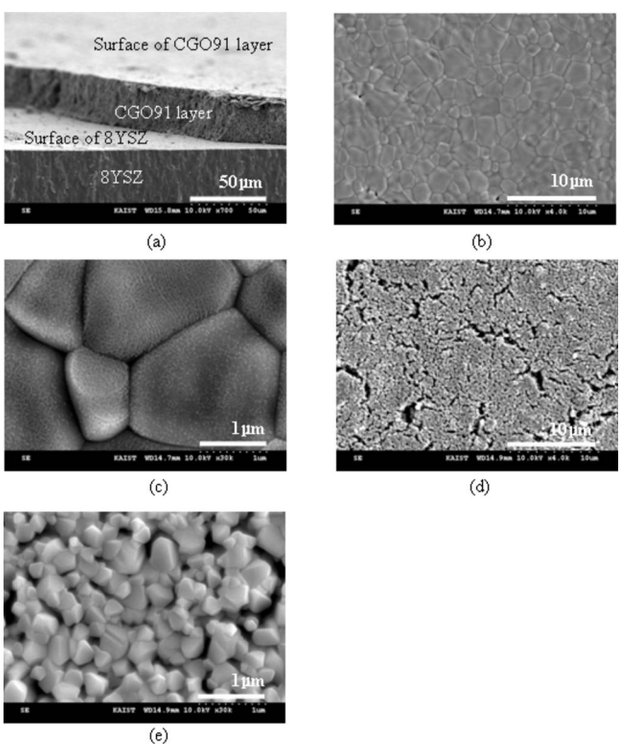

Figure 9. SEM images of surface properties of CGO91 buffer layer and 8YSZ. (a) Surface of coated CGO91 buffer layer on dense 8YSZ sintered at 1400°C. (b and c) Surface morphology of 8YSZ. (d and e) Surface morphology of CGO91 used as buffer layer.

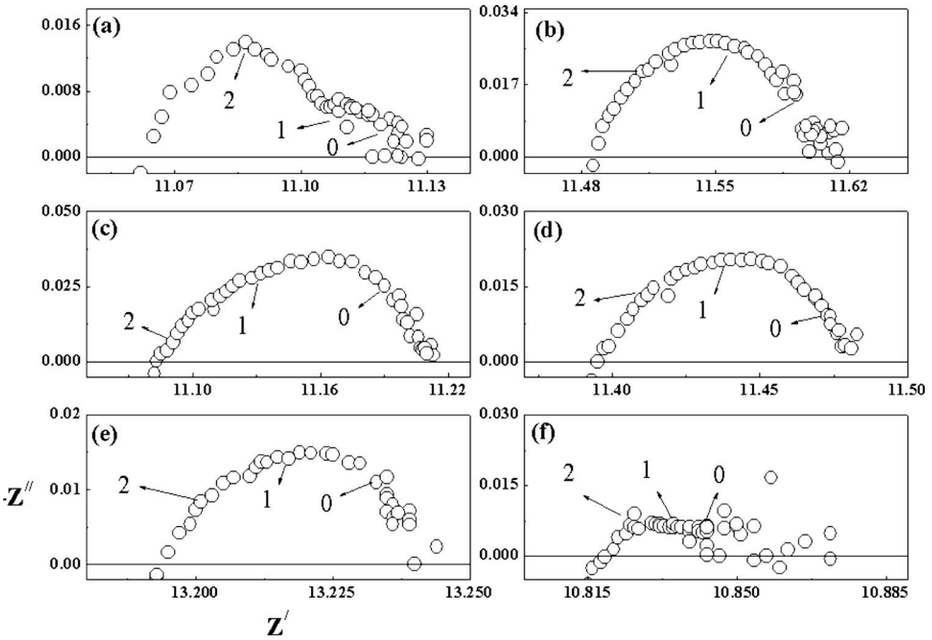

Figure 10. Impedance plots of various composite cathodes: (a) SBSCO, (b) SBSCO10, (c) SBSCO20, (d) SBSCO30, (e) SBSCO40, and (f) SBSCO50 on DLE. The number in each figure shows the order of frequency.

The SEM image in Fig. 12a shows a fracture cross section of SBSCO50 sintered at 1000°C for 1 h on DLE. The SBSCO50, the CGO91 used as buffer layer, and the 8YSZ pellet are in the order from the top, middle, and bottom layer in Fig. 12a. The thicknesses of the SBSCO50 and CGO91 buffer layers were about 25 μm, respectively. In the case of relative porosity, SBSCO50 shows a higher porosity when compared to the buffer layer and 8YSZ. The SBSCO50 layer is shown in detail in Fig. 12b and reveals a range of particle sizes for the SBSCO powder between approximate values of 1–5 μm, with submicrometer CGO91 grains and agglomerates on the surface of the SBSCO grains. Figure 12c shows the cross section of the CGO91 buffer layer and 8YSZ electrolyte, which can be seen to contain microporosity. This may form a high-surface-area interface to the SBSCO cathode, leading to enhanced cathode performance, and may in part explain the earlier observation that an electrode on the DLE had a higher performance than one on a single-phase pressed CGO91 electrolyte.

Thermal expansion curves and CTE with increasing temperature for SBSCO and the SBSCO:CGO91 composites are given in Fig. 13a and b, respectively. Changes in the slope for the expansion curves of SBSCO, SBSCO10, SBSCO20, SBSCO30, and SBSCO40 were observed in the vicinity of 300°C and for SBSCO50 at 400°C. When comparing CTE results at 500 and 700°C, the values of SBSCO and the composites from SBSCO10 to SBSCO50 are 20.3, 18.6, 16.3, 16.0, 15.1, and 12.6 × 10^{-6} K^{-1}, respectively, at 500°C and 21.9, 19.7, 17.1, 16.7, 15.6, and 13.6 × 10^{-6} K^{-1} at 700°C. Significantly, the CTE from SBSCO50 at 500 and 700°C was reduced to around 60% of the SBSCO value, and these results are close to the CTE values of CGO91.[27]

The change in the curve in the vicinity of 300°C can be related to the generation of oxygen vacancies. Similar behavior is observed $(Ba,Sr)(Fe,Co)O_{3-\delta}$ which also shows discontinuities in the expansion curve at 300°C.[28] The similarities in the behavior of SBSCO and $(Ba,Sr)(Fe,Co)O_{3-\delta}$ suggest that enhanced concentration of oxygen vacancies may be expected in SBSCO at lower temperatures. It is a concern that this may result in an unstable phase state in SBSCO; however, this may be mitigated by using the concept of the composite cathode. The results presented in Fig. 13 show that using composite cathodes not only reduces the thermal expansion curve and CTEs but also minimizes the discontinuities in the curve.

The results obtained in this work for SBSCO50 on the DLE are compared to ASR values of other contemporary IT-SOFC cathodes

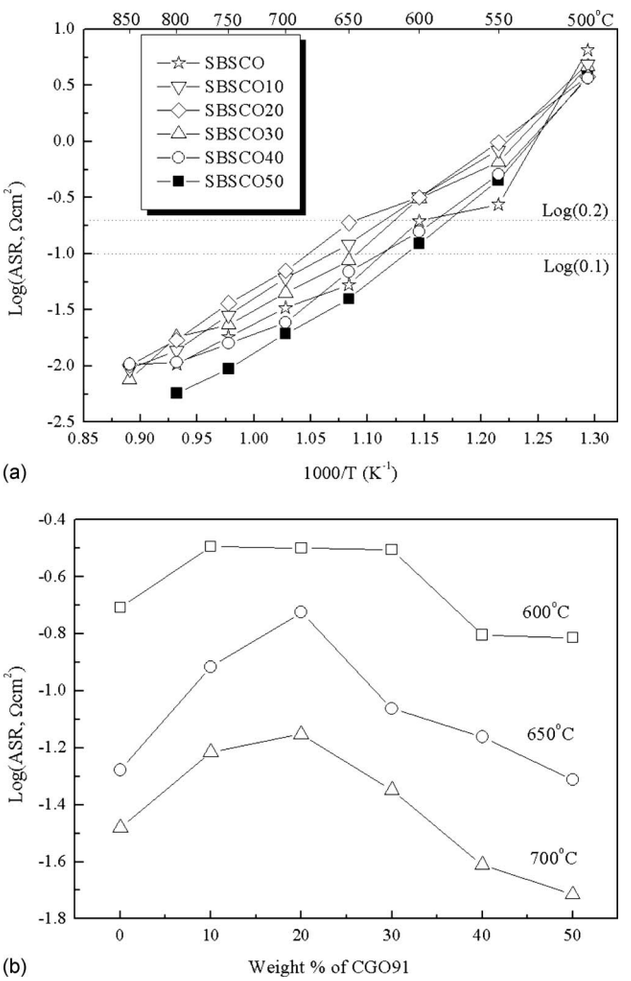

Figure 11. (a) ASR results of composite cathode materials on DLE and (b) ASR results as a function of weight percentages of CGO91 as composite cathode from 600 to 700°C.

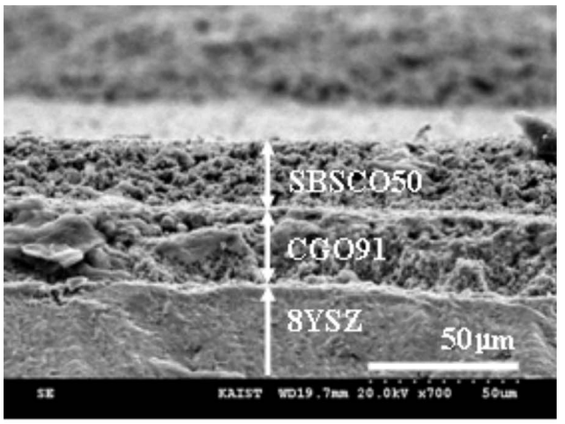

(a)

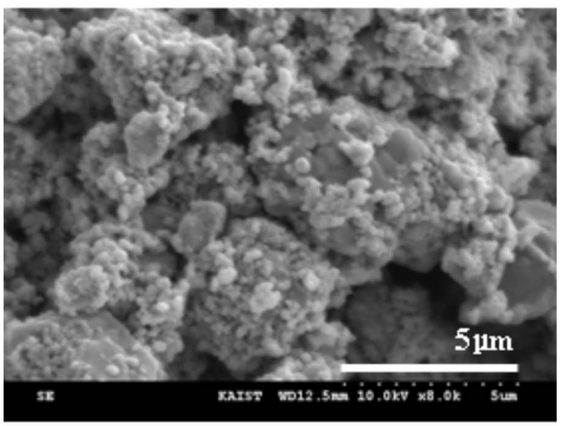

(b)

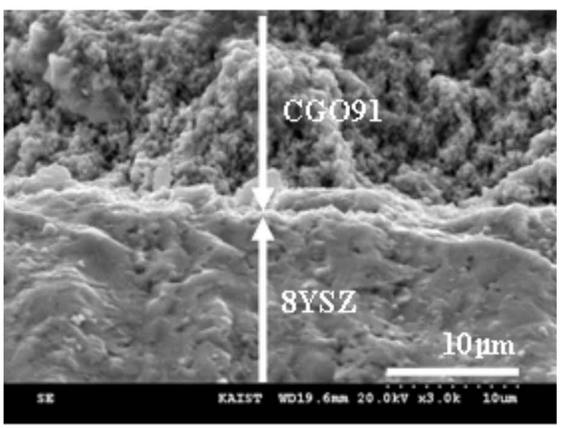

(c)

Figure 12. Morphology of SBSCO50 on DLE with SEM measurement. (a) Image of cathode (SBSCO50), coated layer (CGO91), and dense pellet (8YSZ) showing symmetric cells, (b) the cathode part (SBSCO50), and (c) the results of DLE (porous layer is coated layer with CGO91 on 8YSZ).

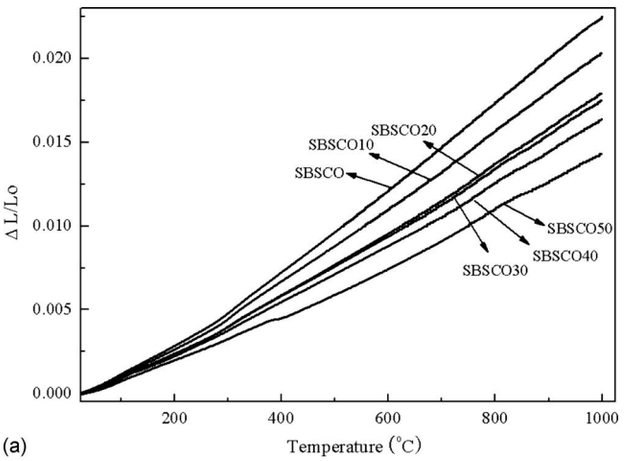

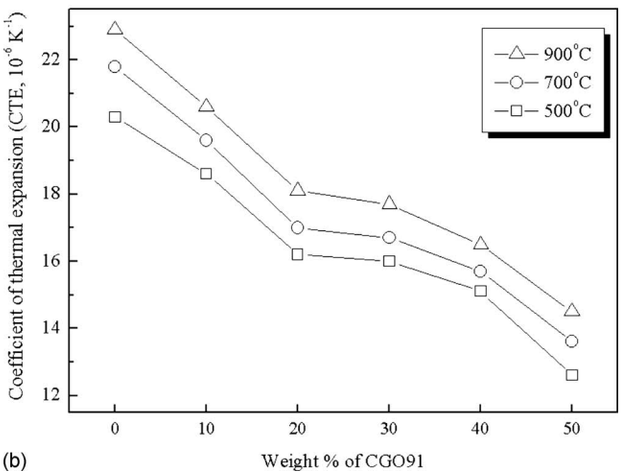

Figure 13. (a) Thermal expansion curves and (b) CTEs as a function of weight percentages of CGO91 from room temperature to 500, 700, and 900°C.

from literature[25,26] (Fig. 14). The ASRs of $Pr_{0.5}Sr_{0.5}CoO_{3-\delta}$ (PSC55) and $Gd_{0.5}Sr_{0.5}CoO_{3-\delta}$ (GSC55) on DLE were 0.55 and 0.35 Ω cm^2, respectively, at 700°C.[25] Comparing these results with SBSCO50, a difference of 1 order of magnitude is observed. Further, the ASR of $Sm_{0.5}Sr_{0.5}CoO_{3-\delta}$ (SSC55) was cited as 0.036 Ω cm^2 at 700°C.[26]

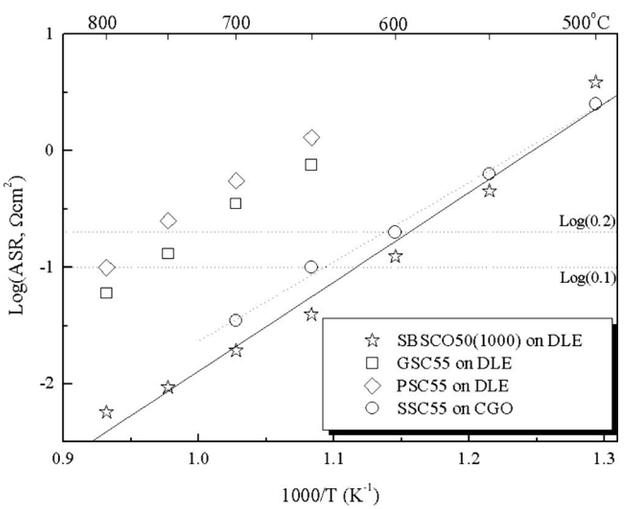

Figure 14. Comparison of ASR. The white open diamond and square results were from PSC55 and GSC55,[27] and the white star was from SSC55.[28] The dot slope came from the ASR values of SSC55 and line slope from SBSCO50.

This compares well the value of 0.019 Ω cm^2 at 700°C reported in this experiment. This indicates that SBSCO50 shows sufficient electrochemical performance to make it a serious candidate for IT-SOFC cathode applications.

Conclusion

In this research, $LnBa_{0.5}Sr_{0.5}Co_2O_{5+\delta}$ (Ln: Pr, Sm, and Gd) was studied as a possible cathode material for IT-SOFC. This oxide has an LP structure into which Sr was substituted for the original lanthanide cation structure. XRD analysis revealed that the subcell was pseudotetragonal when Pr was the original lanthanide However, a much larger orthorhombic distortion is observed when Sm and Gd were the original lanthanides. The crystallographic structure will be studied in more detail using neutron diffraction in the future.

The optimum sintering temperature of $LnBa_{0.5}Sr_{0.5}Co_2O_{5+\delta}$ (Ln: Pr, Sm, and Gd) was suggested as 1000°C for 1 h. The ASR of SBSCO on CGO91 was 0.09 Ω cm^2 at 700°C. Electrochemical analysis of SBSCO with different electrolyte types showed that the best ASR value was SBSCO on the DLE with a value of 0.033 Ω cm^2 at 700°C, showing a lower ASR than when used directly on a CGO91 electrolyte. Composite cathodes of CGO91 and SBSCO showed minimum ASR values at 50 wt % CGO91, with an ASR value of 0.019 Ω cm^2 at 700°C again on the DLE. The microstructure of both the composite cathode and the CGO91 buffer layer contribute significantly to the excellent ASR of the cathode, and further development and long-term stability will be closely linked to these physical attributes.

The CTEs of SBSCO were 20.3 and 21.9 $\times$ 10^{-6} K^{-1} at 500, and 700°C respectively, with the CTEs of the SBSCO50 composite being 12.6 and 13.6 $\times$ 10^{-6} K^{-1} over the same temperature ranges. The decreased CTE by using the composite cathode is similar to the value of CGO91.

Overall performance of the SBSCO50 composite on the DLE is comparable with other contemporary cathodes for IT-SOFC, and therefore this material is a serious candidate for these applications. The use of the 8YSZ-based DLE also opens interesting possibilities for the use of this material at higher temperatures, where it may facilitate the efficient operation of the SOFC at higher cell voltages with a possible benefit in degradation. Future work will include further studies on the influence of composition and microstructure on both short-term performance and long-term durability.

Acknowledgments

This work is an outcome of the projects of the development program of Core Technologies for Fuel Cells (CTFC) of the Ministry of Knowledge Economy (MKE) and is supported by the second state of the Brain Korea 21 project. We also thank EPSRC and Carbon Trust for their support of this work.

Korea Advanced Institute of Science and Technology assisted in meeting the publication costs of this article.

References

1. B. C. H. Steel, *Nature (London)*, **400**, 619 (1999).
2. S. C. Singhal, *Solid State Ionics*, **135**, 305 (2000).
3. M. Juhl, S. Primdahl, C. Manon, and M. Mogensen, *J. Power Sources*, **61**, 173 (1996).
4. E. P. Murry and S. A. Barnett, *Solid State Ionics*, **143**, 265 (2001).
5. Y. Takeda, R. Kanno, M. Noda, Y. Tomida, and O. Yamamoto, *J. Electrochem. Soc.*, **134**, 2656 (1987).
6. C. Frontera, J. L. García-Muñoz, A. Llobet, L. Mañosa, and M. A. G. Aranda, *J. Solid State Chem.*, **171**, 349 (2003).
7. M. Respaud, C. Frontera, J. L. García-Muñoz, M. Á. G. Aranda, B. Raquet, J. M. Broto, H. Rakoto, M. Goiran, A. Llobet, and J. Rodríguez-Carvajal, *Phys. Rev. B*, **64**, 214401 (2001).
8. A. Chang, S. J. Skinner, and J. A. Kilner, *Solid State Ionics*, **177**, 2009 (2006).
9. G. Kim, S. Wang, A. J. Jacobson, L. Reimus, P. Brodersen, and C. A. Mims, *J. Mater. Chem.*, **17**, 2500 (2007).
10. J. Canales-Vázquez, J. T. S. Irvine, and W. Zhou, *J. Solid State Chem.*, **177**, 2039 (2004).
11. A. McKinlay, P. Connor, J. T. S. Irvine, and W. Zhou, *J. Phys. Chem. C*, **111**, 19120 (2007).
12. A. Maignan, C. Martin, D. Pelloquin, N. Nguyen, and B. Raveau, *J. Solid State Chem.*, **142**, 247 (1999).
13. I. O. Troyanchuk, N. V. Kasper, D. D. Khalyavin, H. Szymczak, R. Szymczak, and M. Baran, *Phys. Rev. B*, **58**, 2418 (1998).
14. R. D. Shannon, *Acta Crystallogr.*, **A32**, 751 (1976).
15. H. Yokokawa, N. Sakai, T. Kawada, and M. Dokiya, *J. Electrochem. Soc.*, **138**, 2719 (1991).
16. F. M. Figueiredo, J. A. Labrincha, J. R. Frade, and F. M. B. Marques, *Solid State Ionics*, **101–103**, 343 (1997).
17. O. Yamamoto, Y. Takeda, R. Kanno, and M. Noda, *Solid State Ionics*, **22**, 241 (1987).
18. N. Q. Minh, *J. Am. Ceram. Soc.*, **76**, 563 (1993).
19. C. Peters, A. Weber, and E. Ivers-Tiffée, *J. Electrochem. Soc.*, **155**, B730 (2008).
20. J. Yang, W. Yue, X. Bo, X. Yi, and Q. Yitai, *Mater. Chem. Phys.*, **74**, 234 (2002).
21. S. Natsuko, K. Haruo, Y. Katsuhiko, H. Teruhisa, B. Manuel E and Y. Harumi, *J. Electrochem. Soc.*, **154**, B1331 (2007).
22. H. Akifusa, H. Natsuro, T. Koichi, S. Kazuyoshi, A. Hiroya, and N. Makio, *Solid State Ionics*, **177**, 2967 (2006).
23. B. C. H. Steele and Angelika Heinzel, *Nature (London)*, **414**, 345 (2001).
24. M. Sahibzada, S. J. Benson, R. A. Rudkin, and J. A. Kilner, *Solid State Ionics*, **113–115**, 285 (1998).
25. C. Rossignol, J. M. Ralph, J.-M. Bae, and J. T. Vaughey, *Solid State Ionics*, **175**, 59 (2004).
26. C. Chun-Liang, H. Ching-Shiung, and H. Bing-Hwai, *J. Power Sources*, **179**, 734 (2008).
27. V. V. Kharton, F. M. Figueiredo, L. Navarro, E. N. Naumovich, A. V. Kovalevsky, A. A. Yaremchenko, A. P. Viskup, A. Carneiro, F. M. B. Marques, and J. R. Frade, *J. Mater. Sci.*, **36**, 1105 (2001).
28. B. Wei, Z. Lü, X. Huang, J. Miao, X. Sha, X. Xin, and W. Su, *J. Eur. Ceram. Soc.*, **26**, 2827 (2006).